The Astrophysical Journal, 772:38 (11pp), 2013 July 20 doi:10.1088/0004-637X/772/1/38

SUZAKU VIEW OF THE *SWIFT*/BAT ACTIVE GALACTIC NUCLEI. V. TORUS STRUCTURE OF TWO LUMINOUS RADIO-LOUD ACTIVE GALACTIC NUCLEI (3C 206 AND PKS 0707−35)

Fumie Tazaki[1], Yoshihiro Ueda[1], Yuichi Terashima[2], Richard F. Mushotzky[3], and Francesco Tombesi[3,4]
[1] Department of Astronomy, Kyoto University, Kyoto 606-8502, Japan
[2] Department of Physics, Ehime University, Matsuyama 790-8577, Japan
[3] Department of Astronomy, University of Maryland, College Park, MD 20742-2421, USA
[4] X-ray Astrophysics Laboratory and CRESST, NASA/Goddard Space Flight Center, Greenbelt, MD 20771, USA
Received 2013 January 8; accepted 2013 May 25; published 2013 July 3

ABSTRACT

We present the results from broadband X-ray spectral analysis of 3C 206 and PKS 0707−35 with *Suzaku* and *Swift*/BAT, two of the most luminous unobscured and obscured radio-loud active galactic nuclei (AGNs) with hard X-ray luminosities of $10^{45.5}$ erg s^{-1} and $10^{44.9}$ erg s^{-1} (14–195 keV), respectively. Based on the radio core luminosity, we estimate that the X-ray spectrum of 3C 206 contains a significant (∼60% in the 14–195 keV band) contribution from the jet, while it is negligible in PKS 0707−35. We can successfully model the spectra with the jet component (for 3C 206), the transmitted emission, and two reflection components from the torus and the accretion disk. The reflection strengths from the torus are found to be $R_{\rm torus}(\equiv\Omega/2\pi) = 0.29 \pm 0.18$ and 0.41 ± 0.18 for 3C 206 and PKS 0707−35, respectively, which are smaller than those in typical Seyfert galaxies. Utilizing the torus model by Ikeda et al., we quantify the relation between the half-opening angle of a torus ($\theta_{\rm oa}$) and the equivalent width of an iron-K line. The observed equivalent width of 3C 206, < 71 eV, constrains the column density in the equatorial plane to $N_{\rm H}^{\rm eq} < 10^{23}$ cm^{-2}, or the half-opening angle to $\theta_{\rm oa} > 80^{\circ}$ if $N_{\rm H}^{\rm eq} = 10^{24}$ cm^{-2} is assumed. That of PKS 0707−35, 72 ± 36 eV, is consistent with $N_{\rm H}^{\rm eq} \sim 10^{23}$ cm^{-2}. Our results suggest that the tori in luminous radio-loud AGNs are only poorly developed. The trend is similar to that seen in radio-quiet AGNs, implying that the torus structure is not different between AGNs with jets and without jets.

Key words: galaxies: active – galaxies: individual (3C 206, PKS 0707−35) – X-rays: galaxies

Online-only material: color figures

1. INTRODUCTION

It has been recognized that feedback from active galactic nuclei (AGNs) plays a significant role in the coevolution between galaxies and supermassive black holes (SMBHs) in their centers (for a review see, e.g., Fabian 2012). AGN outflows in the form of jets and winds could expel and heat the gas in the interstellar medium, thus regulating both star formation and mass accretion onto SMBHs. The powerful jets from AGNs can affect the surrounding structure even at the scale of a galaxy cluster. Despite the importance of AGN feedback, several fundamental questions still remain open, such as: what are the physical mechanisms to launch relativistic jets and how the nuclear structure of AGNs with jets (radio-loud AGNs) differs from those without jets (radio-quiet AGNs)?

X-ray observations bring us significant insight into the nuclear structure of AGNs. There are previous works that compare X-ray spectral properties of radio-loud and radio-quiet AGNs. Piconcelli et al. (2008) find rich emission lines in the soft X-ray spectrum of 3C 234, similar to those of radio-quiet AGNs. These lines come from a photoionized plasma, suggesting that the narrow-line region in radio-loud and radio-quiet AGNs has similar geometrical and physical properties. Warm absorbers similar to those found in radio-quite AGNs are also detected from several radio-loud AGNs (Torresi et al. 2012). Tombesi et al. (2010) discover ultra-fast outflows in some radio-loud AGNs, and their features are very similar to those previously observed from radio-quiet AGNs. However, no consensus has yet been firmly established whether or not there are differences between the two populations in their accretion disk structures and circumnuclear environments. To pursue these issues, our teams have been working in *Suzaku* follow-up of hard X-ray-selected radio-loud AGNs (Tazaki et al. 2010, 2011) detected in the *Swift*/BAT survey (Cusumano et al. 2010; Baumgartner et al. 2013).

The torus is a key structure in AGNs, which is considered to be responsible for supplying mass onto SMBHs. It causes obscuration observed in the so-called type-2 AGNs, a major AGN population in the universe (e.g., Ueda et al. 2003). To understand the origin of the torus, it is critical to identify the essential physical parameters that determine its structure. Previous studies, mainly based on the radio-quiet population, suggest that AGN luminosity is one of the most important parameters. The fact that the fraction of obscured AGN is anti-correlated with X-ray luminosity above $L_{\rm X} > 10^{42}$ erg s^{-1} (e.g., Ueda et al. 2003; Hasinger 2008; Burlon et al. 2011) indicates that the solid angle covered by the torus decreases with $L_{\rm X}$. This correlation can also explain the so-called X-ray Baldwin effect (Iwasawa & Taniguchi 1993) that the equivalent width of the iron-Kα line decreases with X-ray luminosity (Grandi et al. 2006; Ricci et al. 2013).

In this paper, we study the spectra of two very luminous radio-loud AGNs, 3C 206 and PKS 0707−35, observed with *Suzaku* and *Swift*/BAT to reveal their nuclear structure. The main purpose is to establish if the correlation of the torus opening angle with luminosity seen in radio-quite AGNs also holds for radio-loud AGNs. For quantitative discussion, we utilize the numerical torus model by Ikeda et al. (2009) to predict the equivalent width of the iron-K line as a function of torus opening angle and column density.

Our targets, 3C 206 and PKS 0707−35, are the most luminous unobscured (type-1) and obscured (type-2) radio-loud AGNs

Table 1
List of Target

Target Name (*Swift* ID)	3C 206 (J0839.6–1213)	PKS 0707−35 (J0709.4–3559)
R.A. (J2000)[a]	08 39 50.62	07 09 14.09
Decl. (J2000)[a]	−12 14 33.9	−36 01 21.8
Redshift	0.198	0.111
Suzaku observation ID	705007010	706008010
Nominal position	HXD	XIS
Start time (UT)	2010-05-08T16:32:34	2011-04-02T02:16:10
End time (UT)	2010-05-10T11:45:10	2011-04-04T01:32:13
Exposure[b] (XIS) (ks)	80.6	81.1
Exposure (HXD/PIN) (ks)	65.6	57.2

Notes.
[a] The position of each source is taken from the NASA/IPAC Extragalactic Database.
[b] Based on the good time interval of XIS-0.

having hard X-ray luminosities of $L_{14-195\,\mathrm{keV}} = 10^{45.5}$ erg s^{-1} and $10^{44.9}$ erg s^{-1}, respectively, among non-blazar type AGNs with fluxes above 2×10^{-11} erg cm^{-2} s^{-1} (14–195 keV) detected in the *Swift*/BAT 58 month survey (Baumgartner et al. 2013). 3C 206 ($z = 0.1979$; Ho & Kim 2009) is a radio-loud quasar, classified as Seyfert 1.2 from the optical spectrum (Véron-Cetty & Véron 2006). The source is located in a cluster of galaxies with the Abell richness class 1 (Ellingson et al. 1989). The observation with the *EINSTEIN* High Resolution Imager detected no significant extended X-ray emission within ∼2 arcmin from the AGN (Hall et al. 1997). The host galaxy of 3C 206 has an elliptical morphology. The black hole mass is estimated to be $M_{\mathrm{BH}} = 10^{8.8-8.9}\ M_{\odot}$ (Sikora et al. 2007; Liu et al. 2006) from the empirical formula using the continuum luminosity at 5100 Å and the line widths of Hα and Hβ. PKS 0707−35 ($z = 0.1108$; Burgess & Hunstead 2006) is a radio galaxy of Fanaroff–Riley type II. This object has a largely extended radio structure up to ∼500″. The galaxy morphology and black hole mass of PKS 0707−35 are not known. We classify this source as an obscured (type-2) object on the basis of the X-ray spectrum, which shows an intrinsic absorption with a hydrogen column density of $N_{\mathrm{H}} > 10^{22}$ cm^{-2} (Section 3.2.2).

This paper is organized as follows. Section 2 summarizes the observations. In Section 3, we present the data analysis and the results including the light curves of *Suzaku* and detailed model fit to the broadband spectra obtained with *Suzaku* and *Swift*/BAT. A summary and discussion are given in Section 4. The cosmological parameters (H_0, Ω_{m}, Ω_{λ}) = (70 km s^{-1} Mpc^{-1}, 0.3, 0.7; Komatsu et al. 2009) are adopted in calculating the luminosities. The errors on the spectral parameters correspond to the 90% confidence limits for a single parameter.

2. OBSERVATIONS

We observed the two radio-loud AGNs 3C 206 and PKS 0707−35 with *Suzaku* on 2010 May 8–10 and 2011 April 2–4, respectively, for a net exposure of ∼80 ks. The hard X-ray fluxes in the 14–195 keV band averaged from 2005 to 2010 (Baumgartner et al. 2013)[5] are 2.5×10^{-11} erg cm^{-2} s^{-1} (3C 206) and 2.2×10^{-11} erg cm^{-2} s^{-1} (PKS 0707−35), which are sufficiently bright for detailed broadband spectral analysis. The basic information of these targets and observation logs are summarized in Table 1.

Suzaku, the fifth Japanese X-ray satellite (Mitsuda et al. 2007), carries three currently active X-ray CCD cameras called the X-ray Imaging Spectrometer (two Front-side Illuminated ones (XIS-FIs), XIS-0, 3, and one Back-side Illuminated one (BI-XIS), XIS-1) and the Hard X-ray Detector (HXD) composed of Si PIN photodiodes and gadolinium silicon oxide (GSO) scintillation counters. We utilize the data of the XIS-FIs, XIS-BI, and HXD/PIN in the energy bands of 1–12 keV, 0.5–8 keV, and 16–35 keV (PKS 0707−35 only), respectively, where the source detection is not affected by the background uncertainties and the calibration is reliable. We do not use the HXD/PIN data of 3C 206 because of the unusually high count rate of the non-X-ray background (NXB) that prevented a firm detection of the source signal.

The data of HXD/GSO, covering above 50 keV, are not utilized, because the fluxes of both targets are too faint to be detected. 3C 206 and PKS 0707−35 were focused on the nominal center position of the HXD and the XIS, respectively. For spectral analysis, we also include the *Swift*/BAT spectra covering the 14–195 keV band averaged over 58 months from 2005 to 2010 (Baumgartner et al. 2013).

3. ANALYSIS AND RESULTS

We reduce the unfiltered event files processed with the versions of 2.5.16.28 (3C 206) and 2.5.16.29 (PKS 0707−35). To reflect the latest energy calibration, we apply the *xispi* ftool with the CALDB files ae_xi{0,1,3}_makepi_20110621.fits. These events files are then screened with standard selection criteria described in the *Suzaku* ABC Guide. To extract light curves and spectra, we use the FTOOLS package (heasoft version 6.11). Spectral fitting is performed with the XSPEC software (version 12.7.0o). The XIS events of each target are extracted from a circular region centered on the source peak with a radius of 3′, and the background is taken from a source-free region within the XIS field of view. We generate the redistribution matrix file (RMF) and ancillary response file (ARF) of the XIS with the *xisrmfgen* and *xissimarfgen* ftools (Ishisaki et al. 2007), respectively. The "tuned" NXB event files provided by the HXD team are utilized for the background subtraction of the HXD/PIN data. The simulated cosmic X-ray background is added to the NXB spectrum based on the formula given by Gruber et al. (1999). We use the HXD/PIN response file ae_hxd_pinxinome9_20100731.rsp. The spectra of *Swift*/BAT and response matrix are available from the HEASARC Web site of the 58 month survey.[6]

[5] http://heasarc.gsfc.nasa.gov/docs/swift/results/bs58mon/

[6] http://heasarc.gsfc.nasa.gov/docs/swift/results/bs58mon/

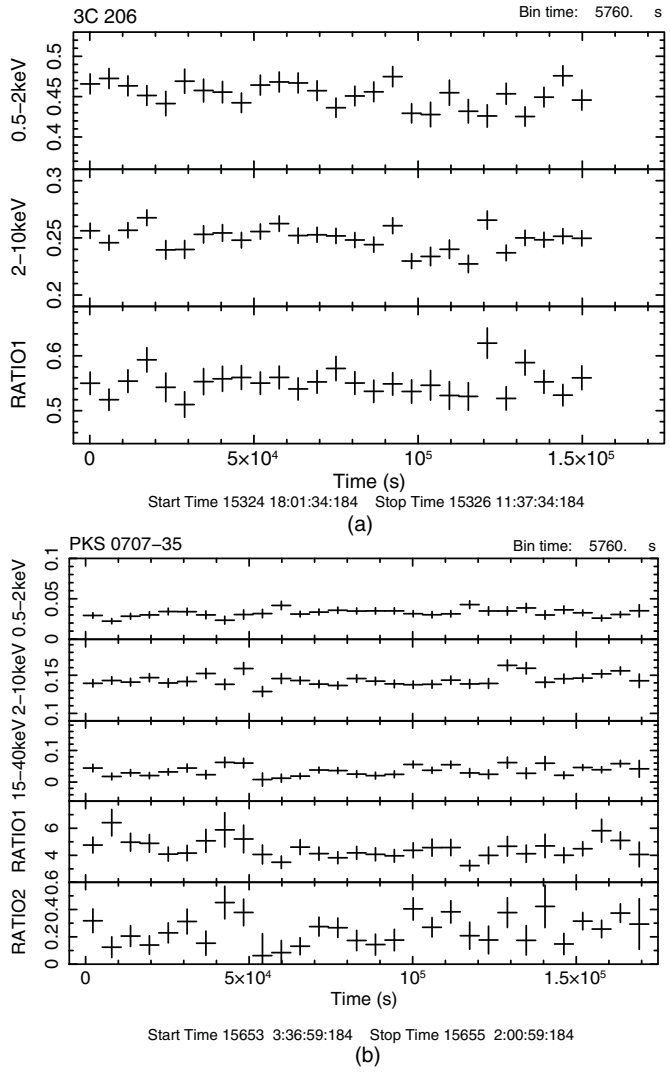

Figure 1. (a) Light curves of 3C 206 in the 0.5–2 keV (upper) and 2–10 keV bands (middle). The lower panel (RATIO1) shows the hardness ratio of 2–10 keV/0.5–2 keV. (b) Light curves of PKS 0707−35 in the 0.5–2 keV, 2–10 keV, and 16–35 keV bands. The lower two panels (RATIO1 and RATIO2) show the hardness ratios of 2–10 keV/0.5–2 keV and 16–35 keV/2–10 keV, respectively.

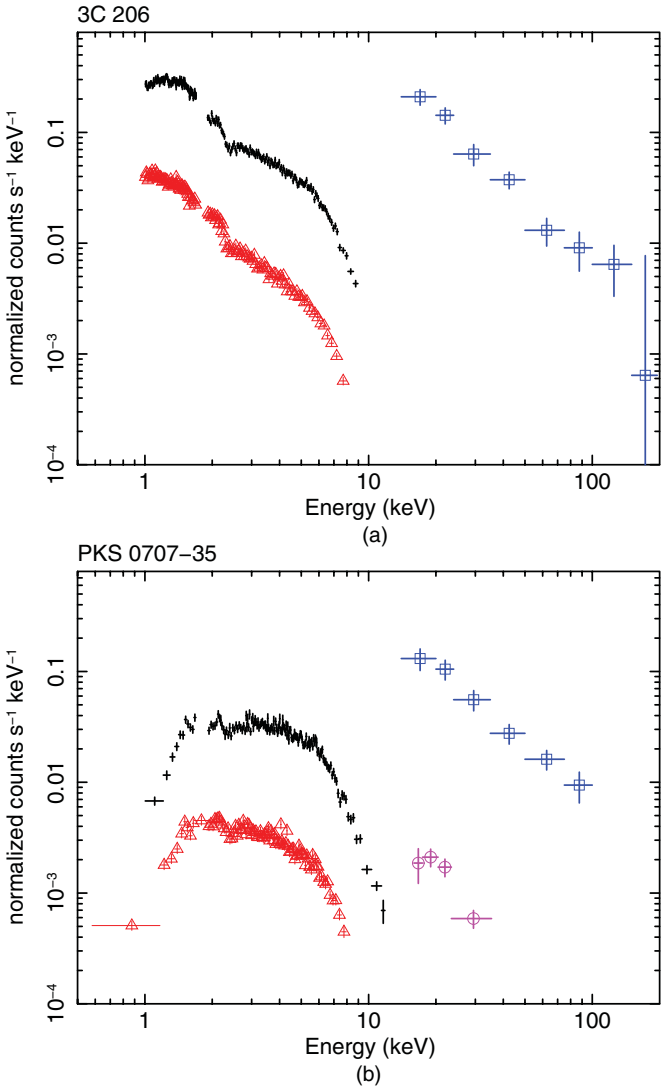

Figure 2. (a) Folded spectra of 3C 206 observed with the *Suzaku* XIS-FIs (black crosses), XIS-BI (red crosses with open triangles), and *Swift*/BAT (blue crosses with open squares). The normalizations of the XIS-BI spectrum are shifted for clarity of the plots. (b) The same for PKS 0707−35. The *Suzaku* PIN spectrum is included (magenta crosses with open circles).

(A color version of this figure is available in the online journal.)

3.1. Light Curves

Figure 1(a) shows the light curve of 3C 206 in the 0.5–2 keV band obtained from XIS-1 (upper), that in the 2–10 keV band combined from XIS-0 and XIS-3 (middle), and the hardness ratio between the two bands (RATIO1). Figure 1(b) represents those of PKS 0707−35, together with the HXD/PIN light curve in the 16–35 keV band. The hardness ratio between the 2–10 keV and 16–35 keV bands (RATIO2) is also plotted. The bin width is 5760 s, the orbital period of *Suzaku*, chosen to eliminate any systematics caused by the orbital change of the satellite. The background is subtracted. As noted from the figures, we find no significant time variability in RATIO1 and RATIO2. Hence, we analyze the time-averaged spectra over the whole *Suzaku* observations for both objects.

3.2. Spectral Analysis

In the spectral analysis, we simultaneously fit the *Suzaku* and *Swift*/BAT spectra. The XIS data in the 1.7–1.9 keV band are excluded because of calibration uncertainties associated with the instrumental Si-K edge. Figure 2 shows the spectra of 3C 206 and PKS 0707−35 folded with the detector response. The relative flux normalization of the XIS-BI to the XIS-FI is set to be a free parameter, while that of the HXD/PIN to the XIS-FIs is fixed at 1.16 for PKS 0707−35 (XIS nominal position), based on the calibration using the Crab Nebula (Maeda et al. 2008). The Galactic absorption, $N_{\rm H}^{\rm Gal}$, is always included in the spectral model with **phabs** in the XSPEC terminology, which is fixed at the value derived from the H I map of Kalberla et al. (2005; $N_{\rm H}^{\rm Gal} = 5.68 \times 10^{20}$ cm^{-2} for 3C 206 and 1.70×10^{21} cm^{-2} for PKS 0707−35). Solar abundances by Anders & Grevesse (1989) are assumed throughout our analysis.

We model the emission from the nucleus (other than the jet component) with a power law with exponential cutoff ($E^{-\Gamma} \times \exp(-E/E_{\rm cut})$) and Compton reflection components from cold matter. Unlike most of previous works, in this paper we consider two reflection components, one from the accretion disk and the other from the torus, in order to achieve a physically consistent picture. Since the direct emission is subject to time

variability between the *Suzaku* and *Swift*/BAT observations, we make the relative normalization of the direct component and its disk reflection ($\mathrm{Norm_{BAT}}$) free between the two spectra. Since we do not anticipate significant time variability in the reflection component from the torus, which usually has a size of an order of ∼0.1 pc or larger (Suganuma et al. 2006), the relative normalization of the torus reflection is tied between the *Suzaku* and *Swift*/BAT observations. In fact, when we apply the formula by Ghisellini & Tavecchio (2008), the torus distances of 3C 206 and PKS 0707−35 are estimated to be ∼2 pc by assuming a bolometric correction factor of $L_{\rm bol}/L_{2-10\,\rm keV} = 30$ for the disk luminosity. For both targets, the cutoff energy is fixed at 200 keV, which is suggested from several radio-loud AGNs (e.g., Grandi et al. 2006; Sambruna et al. 2009). The averaged cutoff energy for local Seyfert galaxies is reported to be ∼300 keV by Dadina (2008), which is somewhat higher than that of radio-loud AGNs. We confirm that the results are little affected even if $E_{\rm cut} = 300$ keV is adopted instead.

To calculate the reflection components, we adopt the **pexmon** model (Nandra et al. 2007) in XSPEC, where the fluorescence lines of iron-Kα, iron-Kβ, and nickel-Kα are self-consistently included in the reflected continuum computed by the **pexrav** code (Magdziarz & Zdziarski 1995). **pexrav** model assumes a neutral, Compton-thick ($N_{\rm H} > 10^{24}$ cm^{-2}) medium with a plane geometry. The relative strength to the direct component is defined by $R \equiv \Omega/2\pi$, where Ω is the solid angle of the reflector viewed from the central irradiating source. We consider the Doppler and relativistic smearing in the disk-reflection component, which is thus modeled as **rdblur * pexmon** in the XSPEC terminology. Since it is difficult to constrain the parameters of **rdblur** from our spectra, we assume the inner and outer radii of the accretion disk to be $100\,r_{\rm g}$ ($r_{\rm g} \equiv GM/c^2$ is the gravitational radius) and $10^5\,r_{\rm g}$, respectively, with a typical emissivity law of r^{-3}. The adopted inner radius can be regarded as a typical value observed from radio galaxies (Tazaki et al. 2010; Sambruna et al. 2009; Larsson et al. 2008), although it is yet uncertain. The inclination angles between the normal axis of the accretion disk and the line of sight are assumed to be 30° for 3C 206 (type-1) and 60° for PKS 0707−35 (type-2). Even when we adopt an inclination angle of 18° for 3C 206 (the lowest available value in the **pexrav**/**pexmon** model), the result of broadband fitting is essentially unaffected. Such a low inclination is unlikely in our case, however, because the predicted jet emission largely overpredicts the observed X-ray flux (see Section 3.2.1 for the details). As for the reflection component from the torus, we ignore any smearing effects, which cannot be resolved at the CCD energy resolution. It is described as a single **pexmon** model, whose inclination angle is fixed at 60° for both targets, as a representable value for the complicated torus geometry.

3.2.1. Broadband Spectral Analysis of 3C 206

Fit without jet component. To evaluate possible contamination of X-ray emission from the galaxy cluster around the AGN, we compare the radial profile of 3C 206 obtained from the XIS-0 and XIS-1 images in the 0.5–2 keV band with that of Mrk 205, an AGN not located in a cluster, observed in 2010 May at the HXD nominal position (*Suzaku* observation ID: 705062010). The results are plotted in Figure 3. There is no evidence for diffuse emission from the cluster of galaxies surrounding 3C 206, which could be extended over ∼600 kpc (∼3′ at $z = 0.1979$). This is consistent with the result by Hall et al. (1997) using *Einstein*. We thus analyze the spectra of 3C 206 by neglecting any emission from the cluster of galaxies.

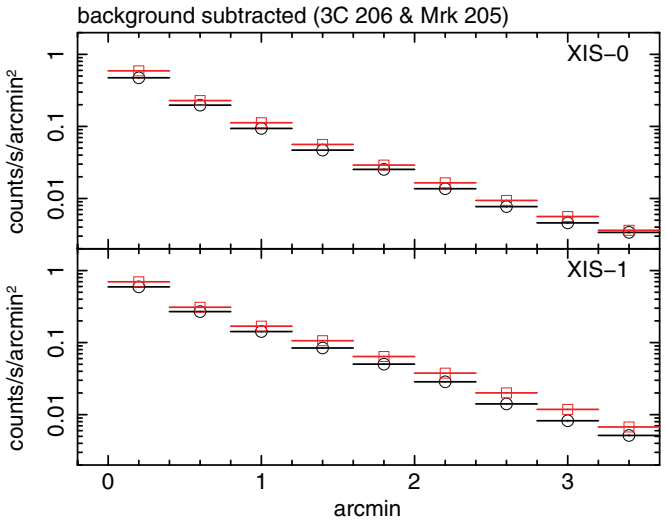

Figure 3. Background-subtracted radial profiles of 3C 206 (black crosses with open circles) and Mrk 205 (red crosses with open squares) obtained from the XIS-0 (upper) and XIS-1 (lower) images in the 0.5–2 keV band.

(A color version of this figure is available in the online journal.)

For the spectral fit of 3C 206, we utilize the data of XIS-FIs in the 1–12 keV band, XIS-BI in the 1–8 keV band, and *Swift*/BAT in the 14–195 keV band; because the XIS spectra show a soft excess below ≈1 keV over a power law extrapolated from higher energies, we do not include the XIS-BI spectrum below 1 keV in the broadband spectral analysis to avoid complexity. Possible origins of the soft excess will be discussed later in this subsubsection. First, we apply a simple model consisting of a direct continuum and its reflection component only from the torus, expressed as *"phabs (constant * zpowerlw * zhighect*[7] *+ pexmon)"* in the XSPEC terminology. Here, the "constant" factor is introduced to represent the time variability between the *Suzaku* and Burst Alert Telescope (BAT) observations. We obtain the best-fit photon index of $\Gamma = 1.75 \pm 0.01$ and reflection strength from the torus of $R_{\rm torus} = 0.25 \pm 0.09$ relative to the time-averaged flux of the direct component determined by *Swift*/BAT with $\chi^2/{\rm dof} = 829.7/825$.

Next, we adopt a model expressed as **"phabs (constant (zpowerlw * zhighect + rdblur * pexmon) + pexmon)"**, adding the reflection component from the accretion disk to the previous model to achieve a physically consistent picture, even though the previous fit without the disk reflection is acceptable in terms of the χ^2 value. Since it is difficult to determine the strengths of the two reflection components independently from our data, we fix only that of the disk component. According to the calculation by George & Fabian (1991), the equivalent width of the iron-K line is predicted to be $\mathrm{EW_{disk}} = 17$–31 eV for an accretion disk truncated at $100\,r_{\rm g}$ for a power-law photon index of 1.7–1.9. Here, we assume an inclination angle of 30° and scale height of the irradiating source of 10 $r_{\rm g}$. We then estimate the corresponding reflection strength of $R(\equiv \Omega/2\pi) \sim 0.1$ in the **pexmon** model so that the predicted equivalent width (17–31 eV) is consistently reproduced. Thus, we fix $R = 0.1$ for the reflection component from the accretion disk. We find that the *Suzaku* and BAT spectra of 3C 206

[7] In the **zhighect** model, we set the threshold energy above which the exponential cutoff is applied to be zero.

favor this model with $R_{\rm disk} = 0.1$ (χ^2/dof = 825.3/825) over the single reflection model, although the difference in the χ^2 value, $\Delta\chi^2 = 4.4$, is not highly significant. We obtain the best-fit photon index of $\Gamma = 1.75 \pm 0.01$ and reflection strength from the torus of $R_{\rm torus} = 0.16 \pm 0.09$ relative to the time-averaged flux of the direct component determined by *Swift*/BAT.

Fit with jet component. Emission from the jets may be contained in the X-ray spectra of radio-loud AGNs. To estimate the jet contribution in the X-ray band, we utilize the radio luminosity in the AGN core, which is attributable to the emission from the innermost region of the jet. According to the unified scheme of AGNs (Antonucci 1993), radio-loud quasars and radio galaxies are intrinsically the same populations of blazars except that the jet axis is not aligned with the line of sight. Thus, from the observed radio luminosity, we can estimate the broad band spectral energy distribution (SED) of the jet emission in (non-blazar) radio-loud AGNs, by referring to averaged SEDs of blazars given as a function of radio luminosity (the so-called blazar sequence) after correcting for relativistic beaming. The observed SED from an emitter moving with a relativistic velocity of v shifts toward higher frequencies by a beaming factor of δ ($\equiv 1/\gamma(1-\beta\cos\theta)$, where $\beta \equiv v/c$, $\gamma \equiv 1/\sqrt{1-\beta^2}$, and θ is the angular separation from the line of sight), and toward higher luminosities by δ^4 (Section 5.8.1.1 in Beckmann & Shrader 2012). By assuming the inclination angle of $\theta_{\rm inc} = 30^\circ$ and the jet velocity of $\beta = 0.9$–0.99 for type-1 radio-loud AGNs, the beaming factor of 3C 206 is estimated to be $\delta_{\rm 3C206} = 0.5$–2. Typically, $\delta_{\rm blazar} \sim 10$ in blazars (Dondi & Ghisellini 1995). Then, we can convert the SED of typical blazars into that of 3C 206 by multiplying a factor of $\delta_{\rm 3C206}/\delta_{\rm blazar}$ and $(\delta_{\rm 3C206}/\delta_{\rm blazar})^4$ in the frequency and luminosity, respectively.

Using the blazar SEDs given in Donato et al. (2001) and the radio luminosity of 3C 206 ($\nu L_\nu = 2.3 \times 10^{42}$ erg s^{-1} at 5 GHz; Elvis et al. 1994), we find that the intrinsic SED of the jet emission in 3C 206 corresponds to those of the three most luminous blazar classes in Figure 10 of Donato et al. (2001). We estimate that the observed X-ray luminosity from the jet in 3C 206 should be $\nu L_\nu \sim 10^{41.7-42.8}$ erg s^{-1} at 1 keV, which is ∼1%–20% of the total observed flux, and the spectrum is approximated by a power law with a photon index of 1.2–1.4 in the X-ray band below 100 keV. Note that when we assume an inclination angle of $\theta_{\rm inc} = 18^\circ$ ($\delta_{\rm 3C206} = 1.7$–2), the jet luminosity is estimated to be $\nu L_\nu \sim 10^{45.1-45.2}$ erg s^{-1} at 1 keV, which is >10 times higher than the total observed flux.

To take into account the jet emission, we add a power law to the spectral model described above. Considering a large uncertainty in the predicted luminosity of the jet component, however, we fix the photon index at 1.3 but set the normalization to be a free parameter. For simplicity, we also assume that the flux ratio between the jet (power law) and the direct component from the disk (cutoff power law) did not change between the *Suzaku* and *Swift*/BAT observations. The final model, which is shown in Figure 4, is expressed as **"phabs (constant (zpowerlw * zhighect + rdblur * pexmon + zpowerlw) + pexmon)"**, where the constant factor takes account of flux variation between the two observations, and the first to fourth terms represent (1) the direct component, (2) the reflection from the accretion disk, (3) the jet component, and (4) that from the torus, respectively.

We confirm that this model, including the jet emission, well reproduces the broadband spectrum in the 1–200 keV band

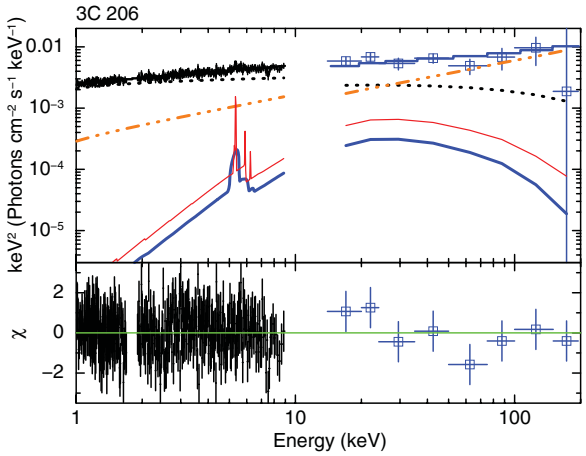

Figure 4. Unfolded spectra of 3C 206 obtained with the XIS-FIs in the 1–12 keV band (black crosses without mark) and *Swift*/BAT in 14–195 keV band (blue crosses with open squares) in units of $EF(E)$ ($F(E)$ is the energy flux at the energy E). The XIS-BI spectrum is not plotted here but is included in the fitting. The top solid curves show the best-fit model (Table 2). The dotted (black), thin solid (red), thick solid (blue), and triple-dot-dashed (orange) curves correspond to the direct component, reflection component from the torus, that from the accretion disk, and jet component, respectively. The residuals in units of σ are plotted in the lower panel.

(A color version of this figure is available in the online journal.)

(χ^2/dof = 818.0/824). Besides the requirement from the consistency with the radio core luminosity, we confirm that the improvement of the fit by adding the jet component is marginally significant with an F-test probability of 99.3%. It is found that the fraction of the jet flux in the total one is ∼20% in the 2–10 keV band and ∼60% in the 14–195 keV band, respectively. This result is consistent with our rough estimate using the radio luminosity and blazar sequence. As for the non-jet emission, we obtain the best-fit photon index of $\Gamma = 1.86^{+0.08}_{-0.07}$ and reflection strength from the torus of $R_{\rm torus} = 0.29 \pm 0.18$. The best-fit parameters are summarized in Table 2. Although the improvement from the previous fit without the jet component is only marginally significant (at 99.3% confidence level from the F-test), we regard this model as the most realistic description of the broadband data of 3C 206, considering that the jet contribution in the X-ray spectrum is quite likely.

We check possible systematic errors caused by our assumption on the reflection component from the accretion disk, which is quite uncertain. If we assume 10 $r_{\rm g}$ as the inner radius of the accretion disk instead of $r_{\rm in} = 100\,r_{\rm g}$, we expect a stronger reflection of $R_{\rm disk} \sim 0.5$, which predicts $\rm EW_{disk} = 100$–130 eV, based on the calculation by George & Fabian (1991). Adopting $r_{\rm in} = 10\,r_{\rm g}$ and $R_{\rm disk} = 0.5$ in the above model (including the jet component) yields the best-fit photon index of $\Gamma = 1.88^{+0.07}_{-0.06}$ and reflection strength from the torus of $R_{\rm torus} < 0.27$ with χ^2/dof = 822.7/824. The fit becomes considerably worse but these parameters are still consistent with those obtained in the case of $r_{\rm in} = 100\,r_{\rm g}$ and $R_{\rm disk} = 0.1$ within the statistical errors at the 90% confidence level.

Soft excess. As mentioned above, we detect the soft excess below 1 keV in the XIS-BI spectrum when the above model is extrapolated toward lower energies; when the XIS-BI spectrum in the 0.6–1 keV band is included, the goodness of the fit becomes rather poor with χ^2/dof = 989.6/926. Similar features are observed in the X-ray spectra of many Seyfert 1 galaxies. First, we consider possible contribution of optically thin thermal emission from a gas unrelated to the AGN. By adding the

Table 2
Best-fit Parameters of Broadband Spectra

		3C 206	PKS 0707−35
(1)	$N_{\rm H}^{\rm Gal}$ (10^{22} cm^{-2})	0.0568[a]	0.170[a]
(2)	Norm$_{\rm BI}$	1.02 ± 0.01	0.97 ± 0.02
(3)	Norm$_{\rm PIN}$	...	1.16[a]
(4)	Norm$_{\rm BAT}$	$0.73^{+0.17}_{-0.14}$	$0.83^{+0.19}_{-0.18}$
(5)	$A_{\rm nuc.}$ (photon cm^{-2} s^{-1} keV^{-1})	$3.40^{+0.21}_{-0.18} \times 10^{-3}$	$1.79^{+0.25}_{-0.20} \times 10^{-3}$
(6)	$A_{\rm jet}$ (photon cm^{-2} s^{-1} keV^{-1})	$4.21^{+2.23}_{-2.54} \times 10^{-4}$	...
(7)	$N_{\rm H}^{1}$ (10^{22} cm^{-2})	...	$5.1^{+3.2}_{-2.3}$
(8)	$N_{\rm H}^{2}$ (10^{22} cm^{-2})	...	$2.0^{+0.4}_{-0.9}$
(9)	f	...	$0.41^{+0.43}_{-0.21}$
(10)	Γ	$1.86^{+0.08}_{-0.07}$	$1.66^{+0.07}_{-0.06}$
(11)	$E_{\rm cut}$ (keV)	200[a]	200[a]
(12)	$R_{\rm disk}$	(0.1[a])	(0.2[a])
(13)	$r_{\rm in}$ ($r_{\rm g}$)	100[a]	100[a]
(14)	$R_{\rm torus}$	0.29 ± 0.18 ($0.21^{+0.12}_{-0.10}$)	0.41 ± 0.18 (0.34 ± 0.12)
(15)	$f_{\rm scat}$ (%)	...	1.3 ± 1.2 (1.0 ± 0.9)
(16)	$\Gamma_{\rm jet}$	1.3[a]	...
(17)	F_{2-10} (erg cm^{-2} s^{-1})	1.0×10^{-11} (2.6×10^{-12})	5.6×10^{-12}
(18)	F_{10-50} (erg cm^{-2} s^{-1})	1.8×10^{-11} (8.0×10^{-12})	1.6×10^{-11}
(19)	L_{2-10} (erg s^{-1})	2.8×10^{44} (6.5×10^{43})	2.1×10^{44}
	χ^2/dof	818.02/824	616.31/582

Notes. The errors correspond to 90% confidence level for a single parameter. Both $f_{\rm scat}$ and R are normalized to the flux of the direct component as measured with *Swift*/BAT (*Suzaku*).
(1) The hydrogen column density of Galactic absorption by Kalberla et al. (2005).
(2) Normalization ratio between the XIS-BI and XIS-FI spectra.
(3) Normalization ratio between the HXD/PIN and XIS-FI spectra.
(4) Normalization ratio of the direct component between the BAT and *Suzaku* spectra.
(5) The power-law normalization of the nuclear emission at 1 keV.
(6) The power-law normalization of the jet emission at 1 keV.
(7) Hydrogen column density for the direct component, which covers $(100 \times f)$% in the line of sight.
(8) Hydrogen column density for the direct component, which covers $(100 \times (1 - f))$% in the line of sight.
(9) Covering fraction.
(10) The power-law photon index of the direct component.
(11) The cutoff energy.
(12) The strength of the reflection component from the accretion disk relative to the flux of the direct component as measured with *Swift*/BAT (*Suzaku*), defined as $R \equiv \Omega/2\pi$, where Ω is the solid angle of the reflector.
(13) The assumed inner radius of the accretion disk.
(14) The strength of the reflection component from the torus relative to the flux of the direct component as measured with *Swift*/BAT (*Suzaku*), defined as $R \equiv \Omega/2\pi$, where Ω is the solid angle of the reflector.
(15) The scattered fraction relative to the flux of the direct component as measured with *Swift*/BAT (*Suzaku*).
(16) The power-law photon index of the jet component.
(17) The observed *Suzaku* flux (that of the jet component only) in the 2–10 keV band.
(18) The observed *Suzaku* flux (that of the jet component only) in the 10–50 keV band.
(19) The 2–10 keV intrinsic luminosity (that of the jet component only) obtained with *Suzaku* corrected for the absorption.
[a] The parameters are fixed.

apec model in the XSPEC terminology, the fit is significantly improved (χ^2/dof = 911.1/924) with a temperature of $kT \sim 0.15$ keV and a luminosity of $L^{\rm thermal}_{0.5-2\,{\rm keV}} \sim 4 \times 10^{43}$ erg s^{-1}. However, this luminosity is too high as that from star-forming regions in the host galaxy of AGNs (e.g., Cappi et al. 1999). As mentioned in the previous section, this could not be the hot gas in the galaxy cluster, either. Thus, we conclude that this model is unrealistic, even though it is statistically acceptable.

A possible origin is a thermal Comptonization component of soft seed photons from the disk (e.g., Noda et al. 2011), although the physical picture is not yet established. We find that the **compTT** model (Titarchuk 1994) successfully represents the soft excess (χ^2/dof = 902.6/923 corresponding to an F-test probability of > 99.99%) with the best-fit electron temperature of $kT_{\rm e} \sim 42$ keV and optical depth of $\tau \sim 0.1$ for blackbody seed photons of 0.01 keV. The temperature of this Comptonization corona is consistent with the result from the Seyfert 1 galaxy MCG 6–30–15 obtained by Noda et al. (2011), while the optical depth is smaller. We need to be aware of the degeneracy between the temperature and optical depth, however. The observed flux of this component is 5×10^{-13} erg cm^{-2} s^{-1} in the 0.5–1 keV band.

An alternative explanation of the soft excess is reflection from a mildly ionized disk, which emits strong iron-L lines below 1 keV (e.g., Ross & Fabian 1993; Crummy et al. 2006; Sambruna et al. 2011). Accordingly, we utilize the **reflionx** model (Ross & Fabian 2005; Ross et al. 1999) convolved with **rdblur** (Fabian et al. 1989), instead of "cold" reflection modeled as **rdblur * pexmon**. Since such an ionized disk region is expected to be located close to the SMBH, we fix $r_{\rm in} = 6\,r_{\rm g}$, the

innermost stable circular orbit of a non-rotating black hole. This model also reproduces the soft excess of our spectra with the best-fit ionization parameter $\xi \sim 200$ erg cm^{-1} s^{-1}, which predicts prominent iron-L line features below 1 keV (e.g., Ross & Fabian 1993). We obtain χ^2/dof = 911.0/923 with an F-test probability > 99.99% from the model without the soft-excess component. The reflection strength roughly corresponds to $R \sim 0.4$ as estimated from its continuum flux above 10 keV. While we cannot distinguish which is the more realistic model explaining the soft excess, our results on the reflection from the torus are not affected.

3.2.2. Broadband Spectral Analysis of PKS 0707−35

In the spectral analysis of PKS 0707−35, we use the data of the XIS-FIs in the 1.0–12 keV band, XIS-BI in the 0.6–8 keV band, HXD/PIN in the 16–35 keV band, and *Swift*/BAT in the 14–100 keV band. *Swift*/BAT did not detect positive signals above 100 keV from this source. As described below, the jet component is negligible in the X-ray spectrum of PKS 0707−35. We find the continuum to be subject to an intrinsic absorption with $N_{\rm H} \sim 3 \times 10^{22}$ cm^{-2}, on which we base our classification of this source as an obscured AGN. Previous studies (e.g., Turner et al. 1997) showed that a scattered (or photoionized) component of the direct emission by a gas surrounding the nucleus is almost always observed in the X-ray spectra of absorbed AGNs, including radio-loud ones (e.g., Piconcelli et al. 2008; Tazaki et al. 2011; Grandi et al. 2007; Torresi et al. 2009; Evans et al. 2010; Balmaverde et al. 2012). We thus essentially adopt the same model components as applied to 3C 206 except that (1) no jet component is included, (2) intrinsic neutral absorption is applied to the model components, and (3) a scattered component is added with the same photon index as that of the transmitted one. Regarding the third component, we do not find significant improvement of the fit by adding emission lines expected from a photoionized plasma to the power-law model due to limited statistics and energy resolution of the data.

We confirm the absence of a significant jet flux in the X-ray spectrum of PKS 0707−35 based on the same discussion as for 3C 206. The core radio flux of PKS 0707−35 is measured to be 25 mJy at 2.3 GHz by Jones et al. (1994). Assuming the inclination angle of $\theta_{\rm inc} = 60^\circ$, which is larger than the case of 3C 206 because it is a type-2 AGN, and the jet velocity of $\beta = 0.9$–0.99, we estimate the beaming factor of the jet in PKS 0707−35 to be $\delta = 0.1$–1. By comparison with the SEDs of blazars (Donato et al. 2001), we estimate that the fraction of the jet flux is less than ∼0.3% of the total flux at 1 keV corrected for the absorption.

As in the spectral analysis of 3C 206, we first consider the reflection component only from the torus, adopting a model expressed as **"phabs (constant * zphabs * zpowerlw * zhighect + zphabs * pexmon + $f_{\rm scat}$ * zpowerlw * zhighect)"** in the XSPEC terminology. These terms correspond to the direct component, the reflection component from the torus, and the scattered component, respectively. The constant factor represents the flux variation between the *Suzaku* and BAT observations. We assume that the fluxes of the scattered and torus-reflection components did not vary between the two observations. Since it is difficult to constrain the intrinsic absorption separately for the direct and reflection components that are emitted from different regions, we adopt a same $N_{\rm H}$ value for them. We find that the model can reproduce the broadband spectra of PKS 0707−35 reasonably well (χ^2/dof = 631.0/584) with $\Gamma = 1.55 \pm 0.04$, $N_{\rm H} = (2.5 \pm 0.1) \times 10^{22}$ cm^{-2}, $R_{\rm torus} = 0.61 \pm 0.22$, and $f_{\rm scat} = (4 \pm 1)\%$ (the latter two parameters are defined as those relative to the time-averaged flux of the direct component as measured with *Swift*/BAT).

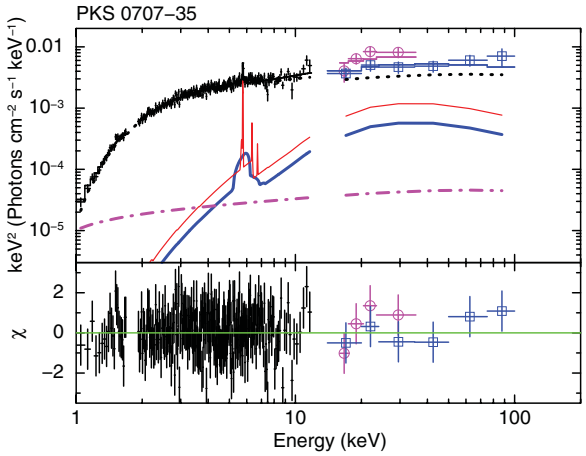

Figure 5. Unfolded spectra of PKS 0707−35 obtained with the XIS-FIs in the 1–12 keV band (black crosses without mark), the HXD/PIN in the 16–35 keV band (magenta crosses with open circles), and *Swift*/BAT in 14–100 keV band (blue crosses with open squares) in units of $EF(E)$. The top solid curves show the best-fit model (Table 2). The dotted (black), thin solid (red), thick solid (blue), and dot-dashed (magenta) curves correspond to the direct component, reflection component from the torus, that from the accretion disk, and scattered component, respectively. The residuals in units of σ are plotted in the lower panel.

(A color version of this figure is available in the online journal.)

Next, we add a reflection component from the accretion disk. The model is thus expressed as **"phabs (constant * zphabs (zpowerlw * zhighect + rdblur * pexmon) + zphabs * pexmon + $f_{\rm scat}$ * zpowerlw * zhighect)"** in the XSPEC terminology, where the second term corresponds to the disk-reflection component. We estimate the strength of the reflection component from the accretion disk by assuming the inner radius of $100\,r_{\rm g}$ and the inclination angle of 60° (instead of 30° as assumed for 3C 206). For a photon index of 1.5–1.8, we find $R_{\rm disk} \approx 0.2$ and ${\rm EW}_{\rm disk} = 13$–26 eV from George & Fabian (1991), and hence we fix $R_{\rm disk} = 0.2$. We find that the fit is better (χ^2/dof = 629.2/584) than the previous one with the same degree of freedom, although the significance of the improvement ($\Delta\chi^2 = 1.8$) is weaker than the case of 3C 206. As expected, we obtain a weaker reflection strength from the torus, $R_{\rm torus} \sim 0.5$, while the other parameters are little changed.

Since the above fit is not yet statistically acceptable, we then adopt a partial covering model instead of a single absorption, where two different absorbing column densities are considered with fractions f and $1 - f$. This model often better reproduces the X-ray spectra of type-2 AGNs (see, e.g., Eguchi et al. 2009). The model, which is shown in Figure 5, is thus expressed as **"phabs (constant * zphabs * zpcfabs (zpowerlw * zhighect + rdblur * pexmon) + zphabs * zpcfabs * pexmon + $f_{\rm scat}$ * zpowerlw * zhighect)"**. We find that the fit is significantly improved (χ^2/dof = 616.3/582) with an F-test probability of 99.76%. The parameters of the partial covering are determined as $N_{\rm H}^1 = 5.1^{+3.2}_{-2.3} \times 10^{22}$ cm^{-2} (41^{+43}_{-21}%) and $N_{\rm H}^2 = 2.0^{+0.4}_{-0.9} \times 10^{22}$ cm^{-2} (59^{+21}_{-42}%). We obtain the best-fit photon index of $\Gamma = 1.66^{+0.07}_{-0.06}$, the reflection strength from the torus of $R_{\rm torus} = 0.41 \pm 0.18$ (to the BAT flux), and the scattering fraction of $f_{\rm scat} = (1.3 \pm 1.2)\%$ (to the BAT flux). The best-fit parameters are summarized in Table 2. We regard this model as the best description of the spectrum of PKS 0707−35.

Finally, we also check systematic uncertainties related to the assumption of the reflection component from the accretion disk. If we assume the inner radius of the accretion disk to be 10 r_g, the calculation by George & Fabian (1991) predicts $R_{disk} \approx 0.9$ and $EW_{disk} = 80$–110 eV for an inclination of 60° and a photon index of 1.5–1.8. Adopting $R_{disk} = 0.9$ and $r_{in} = 10\,r_g$, we obtain the following best-fit parameters with $\chi^2/dof = 614.6/582$: $\Gamma = 1.79 \pm 0.06$, $R_{torus} = 0.44 \pm 0.19$ (to the BAT flux), $f_{scat} = (1.3 \pm 1.2)\%$ (to the BAT flux), $N_H^1 = 4.8^{+2.5}_{-1.9} \times 10^{22}$ cm^{-2} (49^{+35}_{-24}%), and $N_H^2 = 1.9^{+0.4}_{-0.9} \times 10^{22}$ cm^{-2} (51^{+24}_{-35}%). They are all consistent with the case of $r_{in} = 100\,r_g$ within the statistical errors at the 90% confidence level.

3.2.3. Narrowband Spectral Analysis of Iron-Kα Line Features

To confirm the results on the reflection components obtained from the analysis of the broadband spectra, we also analyze the narrowband spectra of the XIS-FIs and XIS-BI in the 3–9 keV and 3–8 keV bands, respectively, focusing on the fluorescence iron-Kα line. Figure 6 plots the spectra of the XIS-FIs. We model the continuum by the same model from which iron-K emission lines are excluded by replacing the **pexmon** model with **pexrav**. A narrow **Gaussian** and a **diskline** component (Fabian et al. 1989) are added, representing iron-K line emission from the torus and accretion disk, respectively. Although iron-K lines from radio-loud AGNs are usually narrow (e.g., Sambruna et al. 2009; Larsson et al. 2008) and hence are likely produced by the torus, here we aim to constrain any possible contribution from the accretion disk directly from our data. Both line energies are fixed at 6.4 keV in the rest frame. In the **diskline** model, the inner and outer radii are fixed at $r_{in} = 100\,r_g$ and $r_{out} = 10^5\,r_g$, respectively, with an emissivity law of r^{-3}. The parameters of the continuum are fixed at those in Table 2 except for the normalization.

The fitting results are summarized in Table 3. Data to continuum model ratio is shown in the lower panel of Figure 6. We find that the observed equivalent widths of the **diskline** component are < 53 eV (3C 206) and < 68 eV (PKS 0707−35), and those of the narrow line are < 30 eV (3C 206) and 58±26 eV (PKS 0707−35), respectively. To discuss the physical origin of these lines, we need to correct the observed equivalent widths for the contribution of the jet in 3C 206. The jet flux accounts for ∼26% of the total flux at 6.4 keV in the rest frame. We thus obtain the equivalent widths of the broad line $EW^{cor1}_{disk} < 71$ eV and the narrow-line $EW^{cor1}_{Gauss} < 40$ eV for 3C 206. Furthermore, for the line originating from the torus, it is necessary to take into account the time variability of the direct component. The equivalent widths of the narrow iron-K line with respect to the five-year averaged BAT flux are found to be $EW^{cor2}_{Gauss} < 71$ eV and 72±36 eV for 3C 206 and PKS 0707−35, respectively, which can be directly compared with theoretical predictions described in Sections 3.2.1 and 3.2.2. These results are consistent with those obtained from the broadband spectra in both targets.

When we assume the inner radius of the accretion disk to be $10\,r_g$, the equivalent widths corrected for the jet contribution and time variability become $EW^{cor2}_{Gauss} = 42 \pm 38$ eV and 79 ± 33 eV and $EW^{cor1}_{disk} < 67$ eV and 115 ± 64 eV for 3C 206 and PKS 0707−35, respectively. These values are still consistent with those derived for the case of $r_{in} = 100\,r_g$. However, the equivalent width of the diskline component in 3C 206 is smaller than the predicted value of 100–130 eV by George & Fabian (1991; see Section 3.2.1). Recalling the fact the model with $r_{in} = 100\,r_g$ better reproduces the broadband spectrum, we infer that the accretion disk of 3C 206 is likely to be truncated at a radius much larger than $10\,r_g$ if the disk produces only cold reflection.

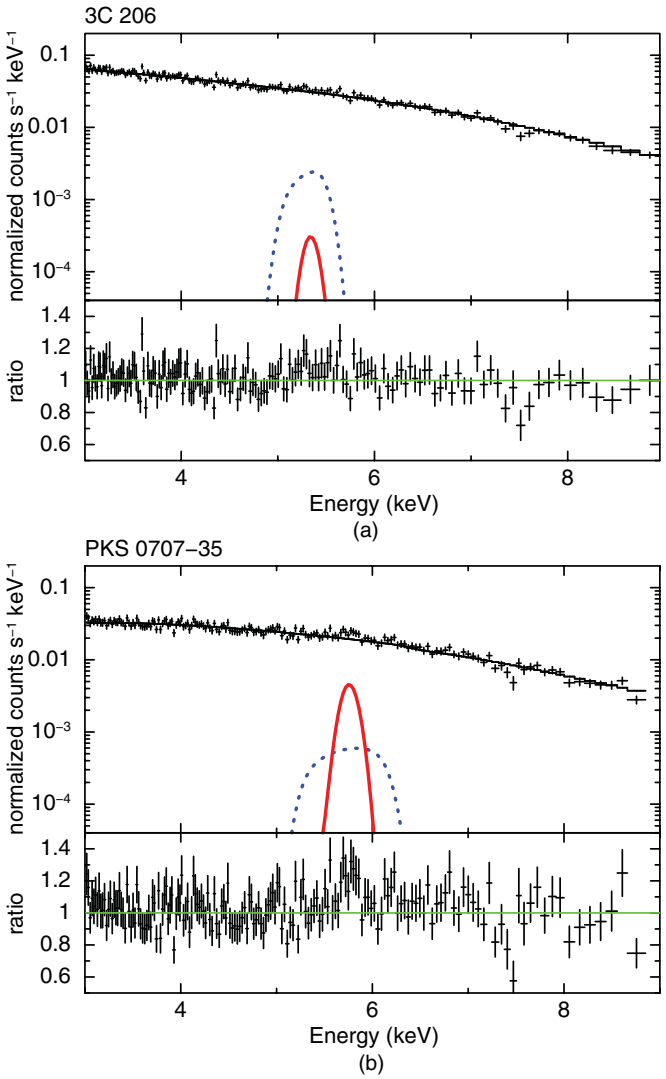

Figure 6. (a) Folded XIS-FI spectrum of 3C 206 in the 3–9 keV band (black crosses). In the spectral fitting, we include the XIS-BI spectrum in the 3–8 keV band, which is not plotted here for clarity. The top solid lines show the best-fit continuum model in Table 2. The best-fit narrow and broad iron-Kα lines are represented with the red solid and blue dotted lines, modeled by a Gaussian and a **diskline** profile, respectively. The ratio between the data and continuum model is plotted in the second panel. Note that the feature around 7.5 keV is instrumental due to a nickel-Kα line in the background spectrum (Tawa et al. 2008). (b) The same for PKS 0707−35.

(A color version of this figure is available in the online journal.)

3.3. Constraining the Torus Structure

Assuming that the narrow iron-Kα line entirely originates from the torus, we can constrain the solid angle and/or hydrogen column density of the torus from the line equivalent width. To quantify the relation between the predicted equivalent width of the iron-K line and torus geometry, we employ the numerical model by Ikeda et al. (2009), where the reprocessed emission from the torus irradiated by the central source is calculated via Monte Carlo simulations.

Ikeda et al. (2009) consider a three-dimensional torus configuration, characterized by the half-opening angle θ_{oa}, the in-

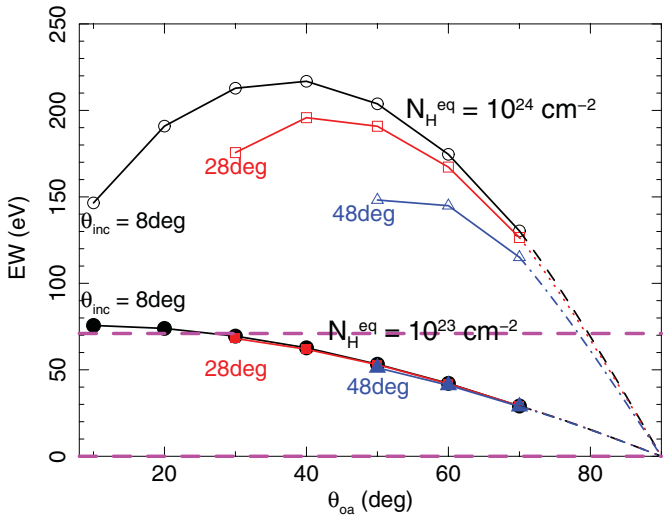

Figure 7. Expected equivalent width of the iron-Kα line to the total continuum given as a function of the opening angle θ_{oa}, calculated from the Monte Carlo simulation by Ikeda et al. (2009). The results are given for two equatorial column densities, $N_H^{eq} = 10^{23}$ (filled marks) and 10^{24} cm^{-2} (opened marks). The circles (black), squares (red), and triangles (blue) represent the results at the inclination angle $\theta_{inc} = 8°$, 28°, and 48°, respectively. In the range between $\theta_{oa} = 70°$ and 90°, the equivalent widths are extrapolated by assuming that the line intensity is proportional to the volume of the torus. The dashed lines (magenta) show the 90% upper and lower limits of the equivalent width obtained from the spectra of 3C 206 when $r_{in} = 100\,r_g$ is assumed for the disk-reflection component (see the text).

(A color version of this figure is available in the online journal.)

Table 3
Best-fit Parameters of *Suzaku* Narrowband Spectra

		3C 206	PKS 0707−35
(1)	E^{cen}_{Gauss} (keV)	6.4[a]	6.4[a]
(2)	σ (eV)	1[a]	1[a]
(3)	E^{cen}_{disk} (keV)	6.4[a]	6.4[a]
(4)	r_{in} (r_g)	100[a]	100[a]
(5)	N_{Gauss} (photon cm^{-2} s^{-1})	($<4.3 \times 10^{-6}$)	$(4.7 \pm 2.1) \times 10^{-6}$
(6)	EW^{obs}_{Gauss} (eV)	(<30)	58 ± 26
(7)	EW^{cor2}_{Gauss} (eV)	(<71)	72 ± 36
(8)	N_{disk} (photon cm^{-2} s^{-1})	($<7.7 \times 10^{-6}$)	($<5.4 \times 10^{-6}$)
(9)	EW^{obs}_{disk} (eV)	(<53)	(<68)
(10)	EW^{cor1}_{disk} (eV)	(<71)	(<68)
	χ^2/dof	312.50/304	389.33/366

Notes. The results of narrowband spectral fitting (3–9 keV for XIS-FIs and 3–8 keV for XIS-BI). The errors correspond to 90% confidence level for a single parameter. If we derive only the upper limit, it is shown in the parenthesis.
(1) The center energy of the narrow iron-Kα line in the rest frame.
(2) The line width for the narrow iron-Kα line.
(3) The center energy of the broad iron-Kα line in the rest frame.
(4) The inner radius of the accretion disk.
(5) The total photon flux of the narrow iron-Kα line.
(6) The observed equivalent width of the narrow iron-Kα line with respect to the *Suzaku* continuum flux.
(7) The corrected equivalent width of the narrow iron-Kα line with respect to the time-averaged continuum flux measured with *Swift*/BAT after subtracting the jet component (in the case of 3C 206). These equivalent widths are written as EW^{cor2}_{Gauss} in the text (see Section 3.2.3).
(8) The total photon flux of the broad iron-Kα line.
(9) The observed equivalent width of the broad iron-Kα line with respect to the *Suzaku* continuum flux.
(10) The corrected equivalent width of the broad iron-Kα line with respect to the *Suzaku* continuum flux after subtracting the jet component (3C 206 only). This equivalent width is written as EW^{cor1}_{disk} in the text (see Section 3.2.3).
[a] The parameters are fixed.

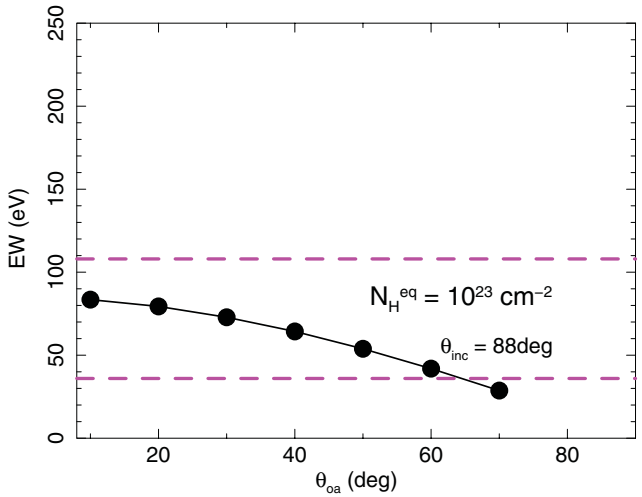

Figure 8. Same as Figure 7, but calculated for type-2 AGNs where the inclination is larger than the opening angle of the torus. $N_H^{eq} = 10^{23}$ cm^{-2} and $\theta_{inc} = 88°$ are assumed. The dashed lines (magenta) show the 90% upper and lower limits of the equivalent width obtained from the spectra of PKS 0707−35 when $r_{in} = 100\,r_g$ is assumed for the disk-reflection component (see the text).

(A color version of this figure is available in the online journal.)

clination angle of the line-of-sight θ_{inc}, the hydrogen column density in the equatorial plane N_H^{eq}, and the ratio between the inner radius r_{in} and outer radius r_{out}, which is fixed at 0.01 (see Figure 2 of Ikeda et al. 2009). A cutoff power law with a cutoff energy of 360 keV is assumed for the spectrum of the central source; this choice little affects the predicted iron-K line intensity when compared with the case of 200 keV. For a photon index of $\Gamma = 1.8$ and a column density of $N_H^{eq} = 10^{23}$ or 10^{24} cm^{-2}, we calculate the iron-K line equivalent widths for various combinations of θ_{inc} and θ_{oa}, using the spectral database available as a "table model" in XSPEC. The results applicable for type-1 AGNs (i.e., $\theta_{inc} < \theta_{oa}$) and for type-2 AGNs (i.e., $\theta_{inc} > \theta_{oa}$) are displayed in Figures 7 and 8, respectively. The inclination is fixed at $\theta_{inc} = 8°$, 28°, or 48° for type-1 AGNs and at $\theta_{inc} = 88°$ for type-2 AGNs.[8] As representative values, we assume $N_H^{eq} = 10^{23}$ or 10^{24} cm^{-2} in Figure 7, and $N_H^{eq} = 10^{23}$ cm^{-2} in Figure 8, the same order of the line-of-sight column density of PKS 0707−35. Although the assumed value of N_H^{eq} more sensitively affects the observed equivalent width in type-2 AGNs than in type-1 AGNs because of absorption of the continuum, the difference in the attenuation fraction of the direct component at 6.4 keV between the line-of-sight column density of 3×10^{22} cm^{-2} (as observed) and 10^{23} cm^{-2} is found to be ∼10% level, which we ignore in the following discussion for PKS 0707−35. Since the Ikeda et al. (2009) model is available only for $\theta_{oa} < 70°$, we extrapolate the result of $\theta_{oa} = 70°$ toward $\theta_{oa} = 90°$ in Figure 7, assuming that the line intensity is proportional to the volume of the torus. The figures show the trend that the equivalent width decreases with increasing half-opening angle except for the case of $N_H^{eq} = 10^{24}$ cm^{-2} in Figure 7, which is consistent with Figure 13 of Ikeda et al. (2009).

In Figures 7 and 8, we also show the range of the "corrected" equivalent width of the narrow iron-Kα of 3C 206 and PKS 0707−35, respectively, with dashed lines. We find that the torus of 3C 206 either has a relatively low column density in the equatorial plane $N_H^{eq} < 10^{23}$ cm^{-2}, or has a large opening angle ($\theta_{oa} > 80°$) if $N_H^{eq} = 10^{24}$ cm^{-2}. Even when we assume 0.5 times smaller elemental abundances for iron and nickel than the solar

[8] The choice of a lower θ_{inc} value for type-2 AGN little changes the result.

values, similar constraints are obtained; $N_{\rm H}^{\rm eq} < 10^{23}$ cm^{-2}, or $\theta_{\rm oa} > 70^{\circ}$ for $N_{\rm H}^{\rm eq} = 10^{24}$ cm^{-2}. The result indicates that the torus of 3C 206 is far from Compton-thick or covers only a small solid angle. The line-of-sight column densities of PKS 0707−35, $N_{\rm H} = (1\text{–}8) \times 10^{22}$ cm^{-2}, suggest a small $N_{\rm H}^{\rm eq}$ for this object, and we confirm that the iron-Kα equivalent width is consistent with the prediction from $N_{\rm H}^{\rm eq} \sim 10^{23}$ cm^{-2} as shown in Figure 8.

4. SUMMARY AND DISCUSSION

4.1. Results Summary

We have obtained the best quality broadband X-ray spectra of the two most luminous radio-loud quasars 3C 206 (type-1) and PKS 0707−35 (type-2) with *Suzaku* and *Swift*/BAT, which have hard X-ray luminosities of $10^{45.5}$ erg s^{-1} and $10^{44.9}$ erg s^{-1} (14–195 keV), respectively. The spectra are well described with a physically motivated model consisting of the direct component (with partial absorptions for PKS 0707−35), its reflection component (including fluorescence lines) from the accretion disk, that from the torus, jet emission (3C 206), and scattered component (PKS 0707−35). Here, we properly take into account the effect of time variability of the direct component between the *Suzaku* and (5 yr averaged) *Swift*/BAT observations. Our main findings are that (1) there is a significant contribution from the jet in the X-ray spectrum only for 3C 206 and that (2) the reflection strength from the torus is estimated to be quite small in both objects compared with typical Seyfert galaxies, which is confirmed by the detailed analysis of the iron-K emission line.

4.2. Jet Contribution to the X-Ray Spectra

We have shown that the X-ray spectrum of the "type-1" radio-loud quasar 3C 206 is likely to contain significant emission from the jet, while its contribution is negligible for the "type-2" radio quasar PKS 0707−35. In the unified scheme of AGNs, radio-loud quasars and radio galaxies are intrinsically the same as blazars except for the inclination angle with respect to the jet axis, which is the smallest in blazars and increases from type-1 to type-2 AGNs. We show that it is possible to make a rough estimate of the contribution from the jet in the X-ray band using the radio core luminosity, by referring to the "blazar sequence" with correction of beaming factor based on reasonable assumptions. Our results imply that non-thermal jet emission may make a significant contribution to the observed X-ray spectrum of type-1 radio-loud AGNs in general, and this component should be taken into account when spectral modeling is done.

The broadband spectral fit suggests that the fraction of the jet component in the X-ray spectrum of 3C 206 is 26% (2–10 keV) and 62% (14–195 keV) of the total flux, which is consistent with the estimate from the radio luminosity within a factor of two If this is the case, the very large hard X-ray luminosity of this source is partially due to the jet emission. The same trend that the relative jet power increases with energy is also reported from 3C 273 (Grandi & Palumbo 2004). The true luminosity arising from the accretion disk is estimated to be 2.2×10^{44} erg cm^{-2} s^{-1} (2–10 keV) and 1.2×10^{45} erg cm^{-2} s^{-1} (14–195 keV), which is very similar to that of PKS 0707−35.

4.3. Reflection Components and Torus Structure

Compton reflection components accompanied by fluorescence lines from matter around the nucleus give us valuable information on the geometry of the surroundings of an AGN. Unlike in most of previous works, we separately consider two reflection components, one from the accretion disk and the other from the torus in order to achieve a physically consistent picture. Relativistic blurring is considered in the disk reflection, whose parameters are linked to the reflection strength in a physically consistent manner, based on the calculation by George & Fabian (1991). Since the torus is located far away from the central SMBH and CCD spectroscopy cannot resolve the line width, we ignore any blurring for the latter. It is hard to distinguish the two reflection components from the spectra alone, which would be strongly coupled with each other in the fitting. Thus, we assume the reflection strength from the accretion disk to be $R_{\rm disk} = 0.1$ (3C 206) and 0.2 (PKS 0707−35), and then derive the reflection strengths from the torus as a free parameter. We obtain $R_{\rm torus} = 0.29 \pm 0.18$ (3C 206) and 0.41 ± 0.18 (PKS 0707−35) from the broadband spectral fitting. These results are consistent with the equivalent widths of the iron-Kα line derived from narrowband (3–9 keV) spectral analysis.

Since any possible broad iron-K line features look very weak in both objects, it is difficult to directly constrain the innermost radius of the accretion disk from the line profile. We find that the broadband fitting of the 3C 206 spectra becomes significantly worse if we assume $r_{\rm in} = 10\,r_{\rm g}$, which predicts a much larger reflection strength from the disk, compared with the case of $r_{\rm in} = 100\,r_{\rm g}$. In addition, the iron-K line analysis in the narrow band yields an upper limit of the equivalent width of a broad iron-K line that is smaller than the prediction by George & Fabian (1991) in the case of $r_{\rm in} = 10\,r_{\rm g}$. These results imply that the accretion disk of 3C 206 is likely to be truncated at a radius much larger than $r_{\rm in} = 10\,r_{\rm g}$ as far as the disk is not significantly ionized. In fact, if we make the disk inner radius a free parameter, by assuming the relation between $r_{\rm in}$ and R based on the equivalent width calculated by George & Fabian (1991) and its corresponding reflection strength in the **pexmon** model (Nandra et al. 2007), then we obtain the best-fit inner radius of $r_{\rm in} = 50^{+90}_{-30}\,r_{\rm g}$. Pictures of truncated disks are obtained from other type-1 radio-loud AGNs, 4C 50.55 ($r_{\rm in} > 340\,r_{\rm g}$; Tazaki et al. 2010), 3C 111 ($r_{\rm in} \sim 20\text{–}100\,r_{\rm g}$; Tombesi et al. 2011), 3C 390.3 ($r_{\rm in} > 20\,r_{\rm g}$; Sambruna et al. 2009), and 4C+74.26 ($r_{\rm in} > 44\,r_{\rm g}$; Larsson et al. 2008). By contrast, the disks of 3C 120 and 3C 382 seem to be extended down to $r_{\rm in} = (9 \pm 1)\,r_{\rm g}$ (Kataoka et al. 2007) and $r_{\rm in} = 12 \pm 2\,r_{\rm g}$ (Sambruna et al. 2011), respectively. It is not clear if there is any systematic trend of disk truncation in radio-loud AGNs. We note that the presence of a highly ionized inner disk extending to $r_{\rm in} = 6\,r_{\rm g}$, or smaller if the black hole is rapidly spinning, cannot be ruled out, however, which might explain the soft excess seen in 3C 206.

Our robust finding is that the reflection component from the torus containing a narrow iron-K line is weak in both 3C 206 and PKS 0707−35 ($R_{\rm torus} < 0.6$) compared with the typical reflection strength observed in the X-ray spectra of Seyfert galaxies ($R \sim 1$; Dadina 2008). Utilizing the torus model by Ikeda et al. (2009), we have quantified the relation between the half-opening angle of a torus ($\theta_{\rm oa}$) and the equivalent width of an iron-K line. The equivalent width with respect to the time-averaged, non-jet continuum flux is < 71 eV for 3C 206. This result constrains that the column density in the equatorial plane $N_{\rm H}^{\rm eq} < 10^{23}$ cm^{-2}, or $\theta_{\rm oa} > 80^{\circ}$ if $N_{\rm H}^{\rm eq} = 10^{24}$ cm^{-2} is assumed, which corresponds to a very small solid angle of $\Omega_{\rm torus}/4\pi < 0.17$. Also, a small value of $N_{\rm H}^{\rm eq}$, $\sim 10^{23}$ cm^{-2}, is inferred for PKS 0707−35 from the line-of-sight absorption column density, which can explain the iron-K

line equivalent width. Thus, these luminous radio-loud AGNs have only poorly developed tori. There is a possibility that the tori are geometrically thick but highly clumpy with a very small filling factor.

It is interesting to compare this result with those obtained from less luminous radio-loud AGNs. Eguchi et al. (2011) analyze *Suzaku* and *Swift*/BAT spectra of the radio galaxy NGC 612, which has $L_{2-10} = 3 \times 10^{43}$ erg s^{-1}, and obtain the equivalent width of a narrow iron-K line of 280 ± 60 eV. They also find that the torus model by Ikeda et al. (2009) well represents the spectra with the best-fit parameters of $N_{\rm H}^{\rm eq} \sim 1.1 \times 10^{24}$ cm^{-2} and $\theta_{\rm oa} \sim 60^\circ$–$70^\circ$. The opening angle of NGC 612 is smaller than the estimate for 3C 206, $\theta_{\rm oa} > 80^\circ$, obtained when a similar value of $N_{\rm H}^{\rm eq} = 10^{24}$ cm^{-2} is assumed. Two narrow-line radio galaxies studied by Tazaki et al. (2011), 3C 403 ($L_{2-10} = 2 \times 10^{43}$ erg s^{-1}) and IC 5063 ($L_{2-10} = 6 \times 10^{42}$ erg s^{-1}), show narrow iron-K line with equivalent widths of 460 ± 100 eV and 150 ± 20 eV, respectively. Thus, the iron-K equivalent widths obtained from type-2 radio-loud AGNs with moderate luminosities are all larger than that of most luminous one PKS 0707−35 ($L_{2-10} = 2.1 \times 10^{44}$ erg s^{-1}). This can be partially explained by their larger line-of-sight column densities that attenuate the continuum fluxes at 6.4 keV: $N_{\rm H} = 1.1 \times 10^{24}$ cm^{-2} (NGC 612), 6.1×10^{23} cm^{-2} (3C 403), and 2.5×10^{23} cm^{-2} (IC 5063).

The comparison suggests that the torus solid angle and/or column density are smaller in more luminous radio-loud AGNs. It is known that the fraction of absorbed AGN decreases with X-ray luminosity above $L_{2-10} \sim 10^{42}$ erg s^{-1} from studies using mostly radio-quiet AGN samples (e.g., Ueda et al. 2003; Hasinger 2008; Burlon et al. 2011). This fact indicates that the solid angle of the torus decreases with luminosity in radio-quiet AGNs. A popular explanation is the receding torus model (Lawrence 1991), where the strong radiation from the central engine affects the structure of the torus; both the solid angle and column density could be reduced in luminous AGNs. Our results are consistent with the idea that the same picture holds for radio-loud AGNs. This implies that the presence of powerful jets is not related to the structure of the torus, which is responsible for gas feeding into the disk as the boundary condition. Rather, some (not yet established) physics taking place in more inner parts of the disk must be involved to explain the difference between radio-loud and radio-quiet AGNs.

We thank the anonymous referee for many useful comments. This work was partly supported by the Grant-in-Aid for JSPS Fellows for young researchers (F.T.) and for Scientific Research 23540265 (Y.U.), and by the Grant-in-Aid for the Global COE Program "The Next Generation of Physics, Spun from Universality and Emergence" from the Ministry of Education, Culture, Sports, Science and Technology (MEXT) of Japan.

REFERENCES

Anders, E., & Grevesse, N. 1989, GeCoA, 53, 197
Antonucci, R. 1993, ARA&A, 31, 473
Balmaverde, B., Capetti, A., Grandi, P., et al. 2012, A&A, 545, A143
Baumgartner, W. H., Tueller, J., Markwardt, C. B., et al. 2013, ApJS, 207, 10
Beckmann, V., & Shrader, C. 2012, Active Galactic Nuclei (Weinheim: Wiley-VCH)
Burgess, A. M., & Hunstead, R. W. 2006, AJ, 131, 114
Burlon, D., Ajello, M., Greiner, J., et al. 2011, ApJ, 728, 58
Cappi, M., Persic, M., Bassani, L., et al. 1999, A&A, 350, 777
Crummy, J., Fabian, A. C., Gallo, L., & Ross, R. R. 2006, MNRAS, 365, 1067
Cusumano, G., La Parola, V., Segreto, A., et al. 2010, A&A, 510, A48
Dadina, M. 2008, A&A, 485, 417
Donato, D., Ghisellini, G., Tagliaferri, G., & Fossati, G. 2001, A&A, 375, 739
Dondi, L., & Ghisellini, G. 1995, MNRAS, 273, 583
Eguchi, S., Ueda, Y., Awaki, H., et al. 2011, ApJ, 729, 31
Eguchi, S., Ueda, Y., Terashima, Y., Mushotzky, R., & Tueller, J. 2009, ApJ, 696, 1657
Ellingson, E., Yee, H. K. C., Green, R. F., & Kinman, T. D. 1989, AJ, 97, 1539
Elvis, M., Wilkes, B. J., McDowell, J. C., et al. 1994, ApJS, 95, 1
Evans, D. A., Reeves, J. N., Hardcastle, M. J., et al. 2010, ApJ, 710, 859
Fabian, A. C. 2012, ARA&A, 50, 455
Fabian, A. C., Rees, M. J., Stella, L., & White, N. E. 1989, MNRAS, 238, 729
George, I. M., & Fabian, A. C. 1991, MNRAS, 249, 352
Ghisellini, G., & Tavecchio, F. 2008, MNRAS, 387, 1669
Grandi, P., Guainazzi, M., Cappi, M., & Ponti, G. 2007, MNRAS, 381, L21
Grandi, P., Malaguti, G., & Fiocchi, M. 2006, ApJ, 642, 113
Grandi, P., & Palumbo, G. G. C. 2004, Sci, 306, 998
Gruber, D. E., Matteson, J. L., Peterson, L. E., & Jung, G. V. 1999, ApJ, 520, 124
Hall, P. B., Ellingson, E., & Green, R. F. 1997, AJ, 113, 1179
Hasinger, G. 2008, A&A, 490, 905
Ho, L. C., & Kim, M. 2009, ApJS, 184, 398
Ikeda, S., Awaki, H., & Terashima, Y. 2009, ApJ, 692, 608
Ishisaki, Y., Maeda, Y., Fujimoto, R., et al. 2007, PASJ, 59, 113
Iwasawa, K., & Taniguchi, Y. 1993, ApJ, 413, 15
Jones, P. A., McAdam, W. B., & Reynolds, J. E. 1994, MNRAS, 268, 602
Kalberla, P. M. W., Burton, W. B., Hartmann, D., et al. 2005, A&A, 440, 775
Kataoka, J., Reeves, J. N., Iwasawa, K., et al. 2007, PASJ, 59, 279
Komatsu, E., Dunkley, J., Nolta, M. R., et al. 2009, ApJ, 180, 330
Larsson, J., Fabian, A. C., Ballantyne, D. R., & Miniutti, G. 2008, MNRAS, 388, 1037
Lawrence, A. 1991, MNRAS, 252, 586
Liu, Y., Jiang, D. R., & Gu, M. F. 2006, ApJ, 637, 669
Maeda, Y., Someya, K., Ishida, M., et al. 2008, JX-ISAS-SUZAKU-MEMO-2008-06
Magdziarz, P., & Zdziarski, A. A. 1995, MNRAS, 273, 837
Mitsuda, K., Bautz, M., Inoue, H., et al. 2007, PASJ, 59, S1
Nandra, K., O'Neill, P. M., George, I. M., & Reeves, J. N. 2007, MNRAS, 382, 194
Noda, H., Makishima, K., Yamada, S., et al. 2011, PASJ, 63, 925
Piconcelli, E., Bianchi, S., Miniutti, G., et al. 2008, A&A, 480, 671
Ricci, C., Paltani, S., Awaki, H., et al. 2013, A&A, 553, A29
Ross, R. R., & Fabian, A. C. 1993, MNRAS, 261, 74
Ross, R. R., & Fabian, A. C. 2005, MNRAS, 358, 211
Ross, R. R., Fabian, A. C., & Young, A. J. 1999, MNRAS, 306, 461
Sambruna, R. M., Reeves, J. N., Braito, V., et al. 2009, ApJ, 700, 1473
Sambruna, R. M., Tombesi, F., Reeves, J. N., et al. 2011, ApJ, 734, 105
Sikora, M., Stawarz, Ł., & Lasota, J.-P. 2007, ApJ, 658, 815
Suganuma, M., Yoshii, Y., Kobayashi, Y., et al. 2006, ApJ, 639, 46
Tawa, N., Hayashida, K., Nagai, M., et al. 2008, PASJ, 60, 11
Tazaki, F., Ueda, Y., Ishino, Y., et al. 2010, ApJ, 721, 1340
Tazaki, F., Ueda, Y., Terashima, Y., & Mushotzky, R. F. 2011, ApJ, 738, 70
Titarchuk, L. 1994, ApJ, 434, 570
Tombesi, F., Sambruna, R. M., Reeves, J. N., et al. 2010, ApJ, 719, 700
Tombesi, F., Sambruna, R. M., Reeves, J. N., Reynolds, C. S., & Braito, V. 2011, MNRAS, 418, L89
Torresi, E., Grandi, P., Costantini, E., & Palumbo, G. G. C. 2012, MNRAS, 419, 321
Torresi, E., Grandi, P., Guainazzi, M., et al. 2009, A&A, 498, 61
Turner, T. J., George, I. M., Nandra, K., & Mushotzky, R. F. 1997, ApJS, 113, 23
Ueda, Y., Akiyama, M., Ohta, K., & Miyaji, T. 2003, ApJ, 598, 886
Véron-Cetty, M.-P., & Véron, P. 2006, A&A, 455, 773